



Quantitative prediction of sub-seismic faults and their impact on waterflood performance: Bozhong 34 oilfield case study

Lei Gong^a, Bo Liu^{b,*}, Xiaofei Fu^{a,b,**}, Hadi Jabbari^c, Shuai Gao^{a,***}, Wenting Yue^{c,d}, Hongqi Yuan^a, Rongzhi Fu^a, Zijie Wang^{c,e}

^a College of Geosciences, Northeast Petroleum University, Daqing, 163318, Heilongjiang, China

^b Institute of Unconventional Oil & Gas, Northeast Petroleum University, Daqing, 163318, Heilongjiang, China

^c Petroleum Engineering Department, University of North Dakota, Grand Forks, 58202, North Dakota, USA

^d Research Institute of Petroleum Exploration & Development, PetroChina, Beijing, 100083, China

^e College of Petroleum Engineering, China University of Petroleum (East China), Qingdao, 266580, Shandong, China

ARTICLE INFO

Keywords:

Sub-seismic faults
Fractal geometry theory
3-D geo-mechanical simulation
Quantitative prediction
Remaining oil

ABSTRACT

Sub-seismic faults are the key factors that control the reservoir quality, hydrocarbon accumulation, and water injection development. In this paper, we developed a method to predict the number, size, orientation and location of sub-seismic faults based on the analysis of fault fractal growth patterns and three-dimensional (3-D) geo-mechanical simulation. This work also discussed the influence of sub-seismic faults on water injection development and remaining oil distribution from analyzing the dynamic oilfield development data. In the methodology developed in this study, the geometrical features of large-scale seismic faults were thoroughly explained based on 3-D seismic data. Based on fractal geometry theory, the number, length and throw of the sub-seismic faults were predicted by extrapolating the power law distribution of seismic fault parameters. According to the distribution of seismic faults, we established the 3-D geo-mechanical model and simulated the disturbed stress field near the seismic fault zone during faulting. By combining the simulation results with the failure criterion, the preferred failure orientation grids and maximum Coulomb shear stress grids were then established. Using these two grids and the parameters of sub-seismic faults constrained by the power-law distribution, we determined the stochastic model to predict the distribution of sub-seismic faults. This work shows that the distribution of sub-seismic faults can be effectively predicted by the combination of fractal theory and 3-D geo-mechanical simulation. Both key parameters in a typical waterflood process, namely the residual oil saturation and the performance of water injection, can be impacted by the size (throw) and the orientation of sub-seismic faults.

1. Introduction

Faults are one of the significant characteristics of a sedimentary basin which usually control the formation and evolution of the basin, the migration and accumulation of hydrocarbons as well as the quality of the reservoirs (Kim et al., 2004; Gudmundsson et al., 2010; Zeng and Liu, 2010; Ferrill et al., 2014; Peacock et al., 2017). Faults can be categorized based on their size and the identification methods into large-scale, medium-scale, and small-scale faults (Fig. 1) (Gauthier and Lake, 1993; Casini et al., 2011; Rotevatn and Fossen, 2011; Laubach et al., 2014). Large-scale faults can be identified by two- or three-dimensional seismic data, i.e. seismic faults (Maerten et al., 2006; Lohr et al., 2008;

Rotevatn and Fossen, 2011). Small-scale faults usually refer to shear fractures that can be identified through cores or imaging logs (Zeng et al., 2013; Sanderson and Nixon, 2015). On the other hand, medium-scale faults may not be identified from seismic or logging data, and they are often referred to as sub-seismic faults (Gauthier and Lake, 1993; Damsleth et al., 1998; Casini et al., 2011; Rotevatn and Fossen, 2011). The boundary between seismic faults and sub-seismic faults is difficult to identify because the depth and lithology may affect the resolution of seismic and logging data (Gauthier and Lake, 1993; Ackermann and Schlische, 1997; Walsh et al., 1998; Steen and Arild, 1999; Fossen and Jonny, 2000; Maerten et al., 2006; Lohr et al., 2008).

Currently, there is no effective method to identify the sub-seismic

* Corresponding author.

** Corresponding author. College of Geosciences, Northeast Petroleum University, Daqing, 163318, Heilongjiang, China.

*** Corresponding author.

E-mail addresses: liubo@nepu.edu.cn (B. Liu), fuxiaofei2008@sohu.com (X. Fu), 349684871@qq.com (S. Gao).

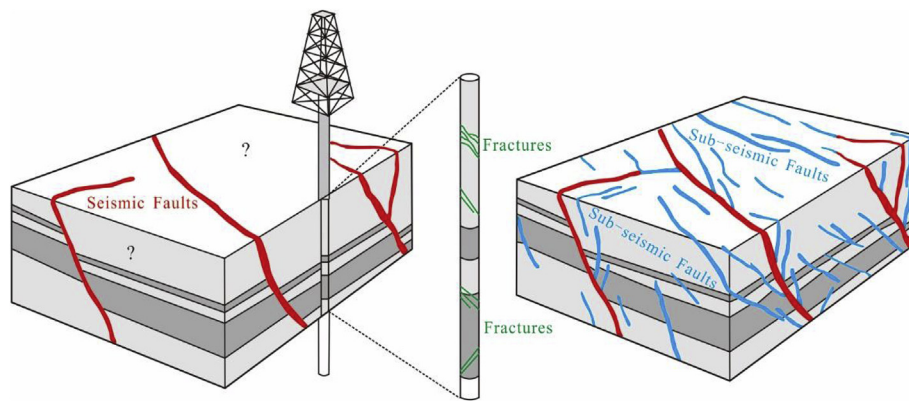


Fig. 1. Schematic diagram showing Seismic faults (red lines, identified through 3-D seismic data), fractures (green lines, perceived through borehole data) and sub-seismic faults (blue lines, hypothetical medium-scale faults, can neither be detected by 3-D seismic data nor by borehole data) (Modified from Maerten et al., 2006). (For interpretation of the references to colour in this figure legend, the reader is referred to the Web version of this article.)

faults even though they have great impacts on the reservoir quality, hydrocarbon accumulation and water injection performance (Damsleth et al., 1998; Rotevatn and Fossen, 2011). Many studies proved that the quantity of sub-seismic faults in a reservoir is far greater than the number of seismic faults (Damsleth et al., 1998; Maerten et al., 2006). The presence of these sub-seismic faults can substantially increase the porosity and permeability of tight reservoirs, making them to be fractured reservoirs, such as the mudstone reservoir of Bristol, UK (Cosgrove, 2001), the Devonian hornstone reservoir in Parkland oil-field, Canada (Packard et al., 2001), and the Triassic pure fractured-tight sandstone reservoir of Dongpu depression, Bohai bay basin, China (Zeng et al., 2013). In addition, when affected by cataclasis, clay smearing, juxtaposition change between sand and clay layers during faulting, and late cementation, the permeability of sub-seismic faults drops sharply, turning them into barriers for the fluid flow in high porosity reservoirs (Fossen and Bale, 2007; Fossen, 2010; Schueller et al., 2013; Meng et al., 2014; Fu et al., 2015; Gong et al., 2017; Luo et al., 2018). In this scenario, they hence damage the lateral continuity and connectivity, and further compromise the water flooding performance. In either case, the sub-seismic faults can strongly control the subsurface fluid flow. Therefore, an accurate prediction of the geometry, development intensity, and location of the sub-seismic faults can provide a reliable geological model for numerical simulation, which can lead to successful deployment of well patterns, exploration, and development plans (Gauthier and Lake, 1993; Maerten et al., 2006).

Many studies show that a fracture system has a power-law distribution (i.e. self-similarity) over a wide range of scales. Therefore, according to fractal theory, the number of sub-seismic faults can be predicted by the fine extrapolation of the power-law distribution of seismic faults parameters (Gauthier and Lake, 1993; Odling, 1997; Marrett et al., 1999; Ortega and Marrett, 2000; Maerten et al., 2006; Gong et al., 2012; Strijker et al., 2012; Hooker et al., 2013, 2014; Wang et al., 2018). However, this method cannot predict the location and orientation of sub-seismic faults. The 3-D geo-mechanical simulation can simulate the stress disturbance near a fault during the fault-creating process. The failure orientations, locations, and density can then be predicted considering the rock failure criteria. In this paper, we predicted the number, length, throw, orientation and location of sub-seismic faults of the Bozhong 34 Oilfield by combining the fractal growth patterns and 3-D geo-mechanical simulation. We also discussed the influence of sub-seismic faults on water injection performance and remaining oil distribution according to the dynamic data from the field development and numerical simulation.

2. Geological setting

Bozhong 34 oilfield locates in the Huanghekou sag in the south of Bohai Bay basin, China (Fig. 2). The overall structure of the oil field is a faulted anticline in NE-SW trending. E-W trending faults and NE-SW trending faults coexist in the studied area (Fig. 3) (Xu et al., 2015).

Based on their orientations, crosscutting and abutting relationships, and the characteristics of tectonic evolution, the nearly E-W trending faults are younger than the NE-SW trending faults. The Paleogene Kongdian Formation (Ek), Shahejie Formation (Es), Dongying Formation (Ed), Neogene Gantao Formation (Ng), Minghuazhen Formation (Nm), and Quaternary Pingyuan Formation (Qp) developed vertically in sequence (bottom to top) in the Bozhong34 oil field (Fig. 3) (Jiang and Pang, 2011). The oil-bearing formation is the Dongying Formation and Shahejie Formation, among which the second Member of Dongying Formation (Ed₂) and the second Member of Shahejie Formation (Es₂) are the major pay zone (Fig. 3).

The burial depth of the second Member of Shahejie Formation (Es₂) is between 3200 m and 3400 m. The bed thickness ranges from 94.6 m to 116.9 m. The sedimentary microfacies is dominated by the main channel and branch channel of fan delta. The fan bodies are large and widely distributed. The lithology is characterized as fine-medium grained arcose and lithic arkose with medium sorting. The porosity is between 11.2% and 17.1% with an average value of 13.1%. The permeability is between 8.9 mD and 449 mD, and the average value is 46.4 mD.

Bozhong 34 oil field started its operation and production in June 1990. And now there are 21 production wells and 5 injection wells in the study area. There is not available technique to effectively identify the small faults in this area due to the inadequate resolution of the seismic data induced by ultra-deep burial depth. Especially, the information about the distribution of sub-seismic faults and their relationship with the remaining oil is still inadequate. Therefore, the quantitative prediction of sub-seismic faults and remaining oil enrichment in Bozhong 34 oilfield is of great significance to resolve production problems and adjust well patterns. The Bozhong 34–2 oilfield is treated as the research target in this case study since it hosts the major production wells in the field (Fig. 3). However, in an effort to obtain more information, all faults in the study area were investigated.

3. Methodology

3.1. Fault fractal growth model

Many studies show that faults and fractures have fractal features. Self-similarity is also found in the process of rock failure. Fractal geometry is widely applied to predict the sub-seismic faults and fractures (Gauthier and Lake, 1993; Marrett et al., 1999; Ortega and Marrett, 2000; Maerten et al., 2006; Fu et al., 2007; Gong et al., 2012). The fault fractal growth model was firstly proposed by King (1983). He concluded that the geometry of the fault is finite in 3-D space; the ideal fault plane is elliptical; the displacement at the center point of the fault is the largest; the displacement gradually decreases from center to the periphery and decreases to zero at the tip line (Fig. 4a and b); the maximum throw and length of faults in the same region follow power law distribution (Fig. 4c):

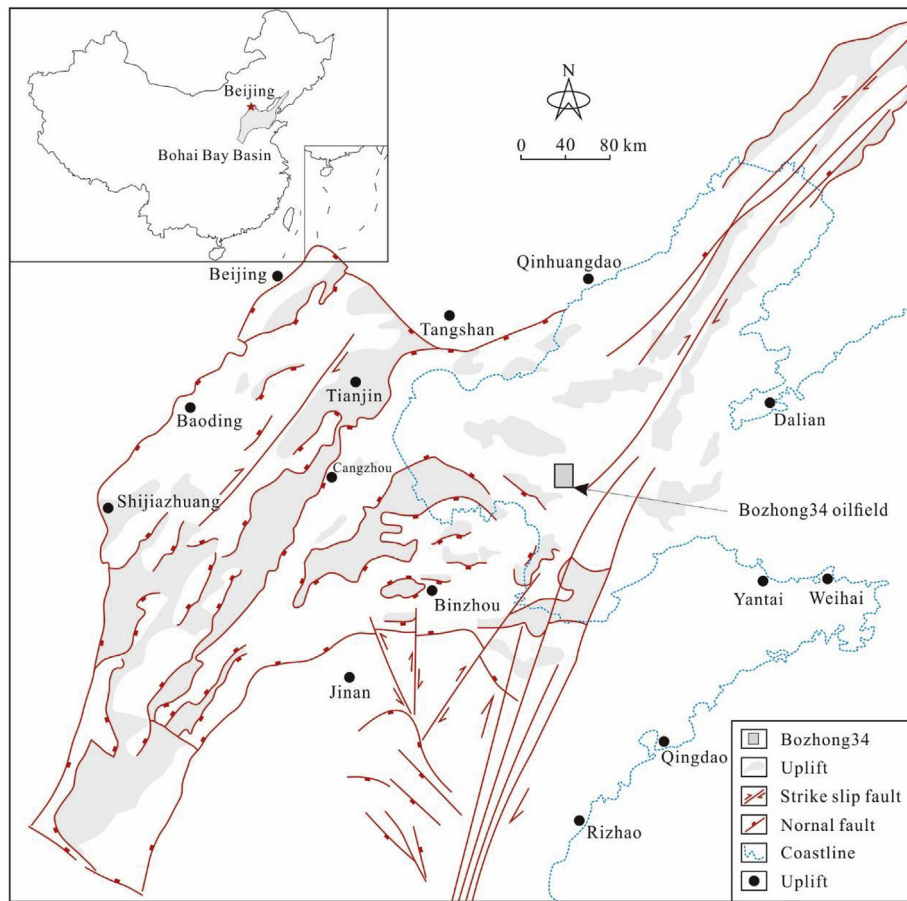


Fig. 2. Tectonic location of Bozhong 34 oilfield and geological map of the Bohai Bay Basin (Modified from Zhao and Li, 2016).

$$D = b_1 \times L^{C_1} \tag{1}$$

Where D is the maximum fault throw, L is the fault length, b_1 is a constant, and C_1 is the power exponent representing the slope of the linear relationship between fault throw and length in the log-log

coordinate. Fault size frequency is also subject to a power law distribution (Fig. 4d):

$$N_L = b_2 \times S^{-C_2} \tag{2}$$

Where N_L is the number of faults with size greater than S , b_2 is a

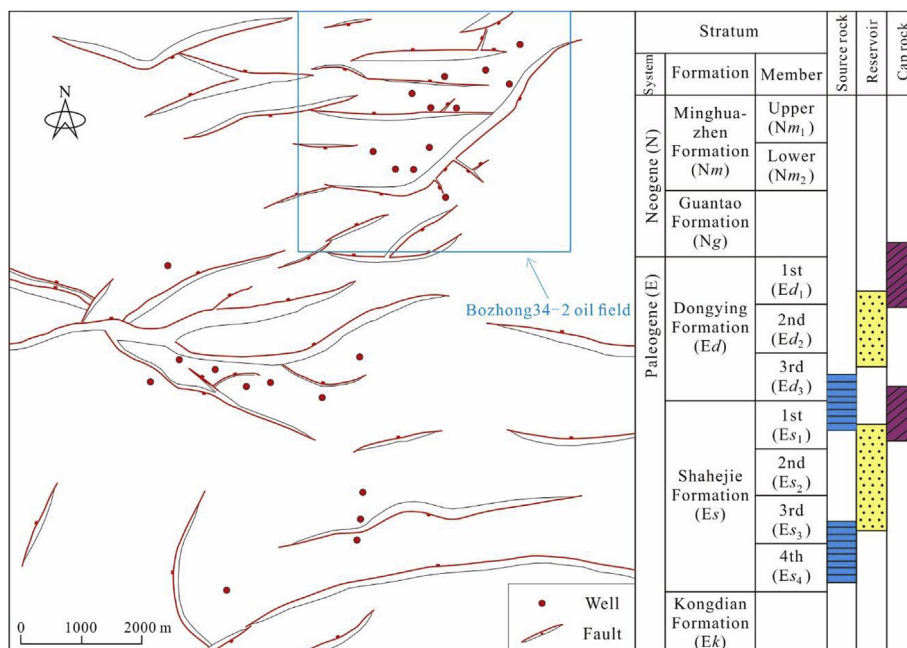


Fig. 3. Fault distribution of the second Member of Shahejie Formation (Es₂) and the assemblages of source rock, reservoir and cap rock in Bozhong 34 oilfield.

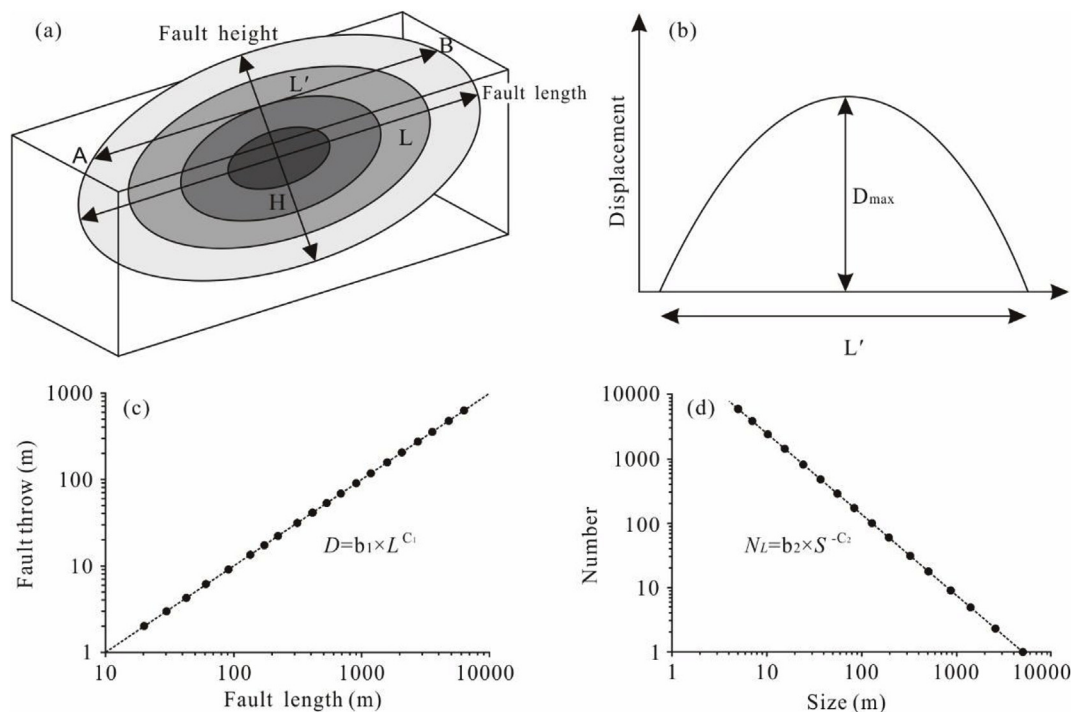


Fig. 4. Fractal model for fault growth (Modified from Barnett et al., 1987, Gauthier and Lake, 1993 and Fu et al., 2012). (a) Ideal contour map of fault throw on fault surface. (b) Ideal displacement profile along AB in Fig. 4a. (c) Ideal relationship between fault length and maximum throw. (d) Ideal relationship between the fault size (length, throw, etc.) and the fault number.

constant, S is fault size (length, throw, etc.), C_2 is the power exponent which represents the slope of linear relationship between frequency and size in the log-log coordinate. Based on this model, we can extrapolate the number and their corresponding size of faults of any scale.

Due to the truncation and censoring effects, the fault size distribution usually seems to follow a log-normal distribution by showing concave shape on both sides, and a straight line in the center segment (Fig. 5). However, according to the studies conducted on fault size-frequency distribution at different scales, the fault size frequency curves should present a power-law distribution rather than a log-normal distribution over a wide range of scales (Gauthier and Lake, 1993; Odling, 1997). For example, Odling (1997) studied the fracture system of the sandstones in western Norway at different scales (Fig. 5a). Although the fracture trace-length mimics a log-normal distribution under a single resolution, they obey a unique power-law distribution with the same exponent of -2.1 when considering all the data. Based on this law, we can establish the relationship between fault size and frequency using the middle straight segment of the fault size frequency distribution obtained from seismic data, and then extrapolate the number and size of sub-seismic faults (Fig. 5b).

3.2. Seismic data analysis

Depth data is needed in the 3-D geo-mechanical simulation, so the seismic data is time-depth converted. A detailed interpretation of the geometry and characteristics of seismic faults are required to establish the fault fractal growth model. For this purpose, we carefully examined and determined the fault length, maximum fault throw, and the occurrence of each fault. We also constrained the displacement distribution of each fault surface. And then these data and seismic horizon data were imported into the Trap Tester software to build the 3-D geological model. Since faults usually exist above and below the target interval, we imported the whole data of each fault into the model to obtain more accurate simulation results.

3.3. 3-D geo-mechanical model

In the process of 3-D geo-mechanical simulation, it is assumed that the formation is homogeneous, isotropic, and linear-elastic material. The mechanical parameters of the rocks are obtained by triaxial rock mechanical experiments. The Boundary Element Method (BEM) is adopted in the simulation. In the BEM method, the boundary surface is discretized while the surrounding materials are not (Maerten et al., 2006). The simulated fault is discretized into triangular elements with specific displacements. This triangular elements in BEM is especially suitable for simulating complex surfaces, such as the curved fault plane with irregular tip lines.

The 3-D geo-mechanical model is controlled by local boundary condition and regional load. The local boundary condition is defined by the displacements of each fault surface. The regional loads can be stresses or strains. Note that, since the studied area experienced multiple tectonic events, each phase had a specific stress field with specific direction and size, which require different sets of boundary conditions. Based on rock mechanical parameters and boundary conditions, the disturbed stress field in any part of the rock mass can be calculated. Then, combined with the failure criterion, the predicted failure strike and density can be obtained. The predicted fault strike is estimated through the Coulomb failure criterion (Maerten et al., 2006), given by:

$$\tan(2\theta) = \pm 1/\mu \quad (3)$$

Where θ is the angle between failure surface and the maximum principal stress σ_1 and μ is the coefficient of internal friction. In 3-D geo-mechanical simulation, we assume that the strata are homogeneous elastomers, and the entire strata have the same rock mechanical parameters. According to the Coulomb shear failure criterion, the probability of a shear failure at a point depends on the shear stress of the potential fault surfaces. The shear stress on this surface is called the maximum Coulomb shear stress (MCSS) (Maerten et al., 2006). Therefore, MCSS value can be used to represent the probability of relative failure at a certain point. The larger the MCSS value is, the

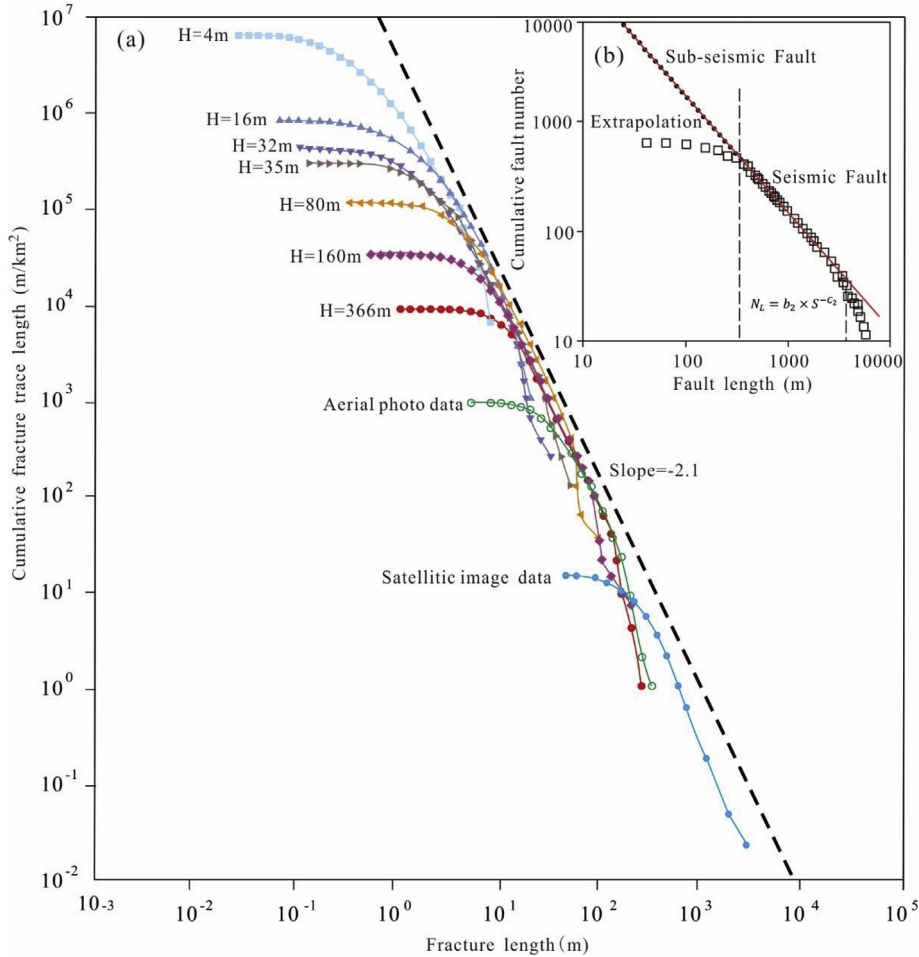


Fig. 5. (a) Cumulative fracture traces length per km² for different scales of fractures (Modified from Odling, 1997). H is the observation height. The higher the H is, the lower the resolution is. Different height represents different scale ranges. All curves of each scales show a log-normal distribution, while when combined all the data together, they obey a power-law distribution with an exponent of -2.1 (the best fitting line is slightly offset to the right for clarity of the plot). (b) Extrapolation the sub-seismic fault information from seismic fault size distribution (modified from Gauthier and Lake, 1993).

greater the chance that failure occurs. The MCSS can be calculated by:

$$MCSS = \frac{\sigma_1 - \sigma_3}{2} \sqrt{1 + \mu^2} - \mu \frac{\sigma_1 + \sigma_3}{2} \quad (4)$$

where σ_1 and σ_3 are the maximum and minimum principal stresses respectively, and μ is the coefficient of internal friction.

3.4. Stochastic modeling of sub-seismic fault

The occurrence and density of sub-seismic faults can be constrained by the 3-D geo-mechanical simulation results. And well data can provide some useful information about sub-seismic faults distribution, but the location of the sub-seismic fault is still unknown. In this paper, the marked-point process stochastic technique was used to determine the location and orientation of sub-seismic faults. The length and number of sub-seismic faults are determined according to the fault-fractal growth model as given in Equation (2). The fault throw of sub-seismic fault is determined by the relationship between fault length and fault throw (Equation (1)). The development positions of sub-seismic faults were determined according to the distribution of the maximum Coulomb shear stress. The orientations of sub-seismic faults were determined by the azimuth of disturbed stress and the Coulomb failure criterion.

4. Case study

In the following case study, we interpreted the horizon and faults

using the 3-D seismic data and summarized the length and maximum throw of each faults. We established the relationship between fault length and the maximum throw as well as the fault length fractal growth model for each set of fault systems based on Equations (1) and (2) (Fig. 6). The actual fault model in the study area is as follows:

The maximum fault throw and length relationship model for the NE-SW trending fault system:

$$D = 0.0056 \times L^{1.2241}, \quad R^2 = 0.9121 \quad (5)$$

The fault length cumulative frequency distribution model for the NE-SW trending fault system:

$$N_L = 15865 \times L^{-0.982}, \quad R^2 = 0.9926 \quad (6)$$

The maximum fault throw and length relationship model for the nearly E-W trending fault system:

$$D = 0.0025 \times L^{1.3714}, \quad R^2 = 0.9251 \quad (7)$$

The fault length cumulative frequency distribution model for the nearly E-W trending fault system:

$$N_L = 722037 \times L^{-1.547}, \quad R^2 = 0.9952 \quad (8)$$

where D is the maximum fault throw, L is the fault length, N_L is the number of faults with fault length longer than L , R is the correlation coefficient.

From Fig. 6a and b, the fault length and maximum throw of both sets of fault systems show good power-law distribution in log-log

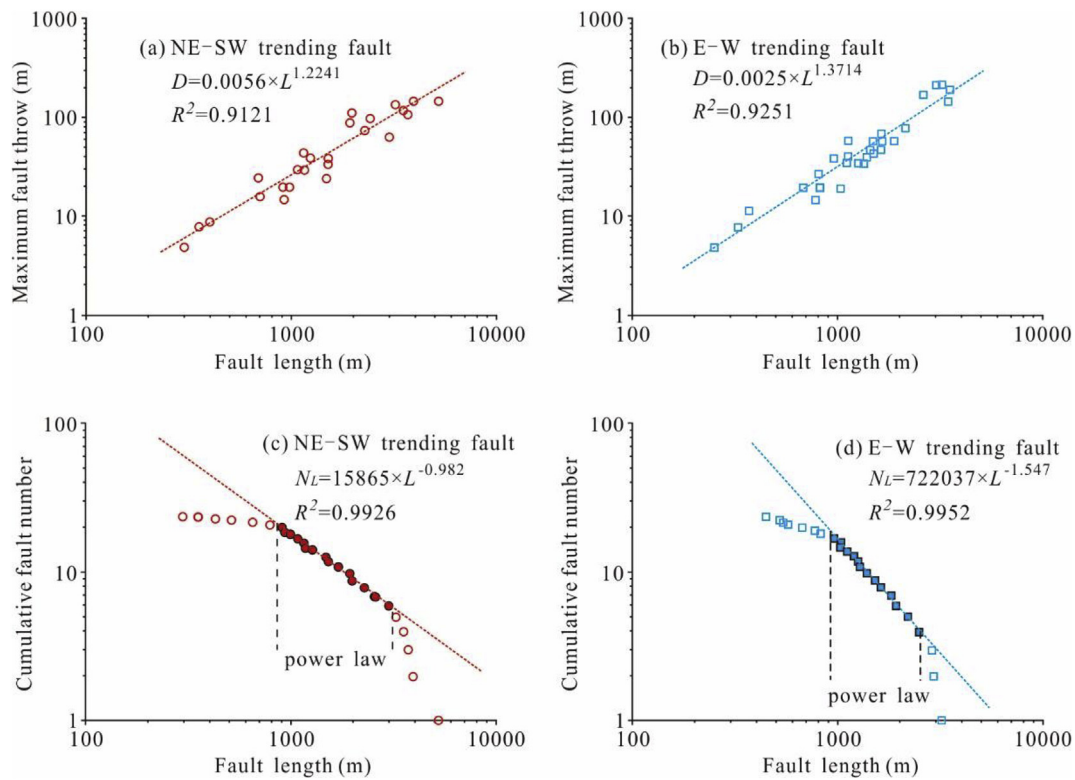


Fig. 6. Fractal model for fault growth of the second Member of Shahejie Formation (Es_2) in Bozhong 34 oilfield.

Table 1

Prediction results of length, throw and number of sub-seismic faults.

NE-SW trending faults			E-W trending faults		
Length (m)	Throw (m)	Number	Length (m)	Throw (m)	Number
900–800	23.1–20.0	2	900–800	28.1–23.9	4
800–700	20.0–17.0	4	800–700	23.9–19.9	6
700–600	17.0–14.1	4	700–600	19.9–16.1	7
600–500	14.1–11.3	5	600–500	16.1–12.6	12
500–400	11.3–8.6	9	500–400	12.6–9.3	20
400–300	8.6–6.0	15	400–300	9.3–6.2	38

coordinate. The fault length cumulative frequency distribution is quite close to a log-normal distribution (Fig. 6c and d), but it presents a linear relationship (power-law distribution) at the center of the data. This is due to the limitation of seismic resolution and boundary effect. Therefore, it is necessary to define two truncations on both sides of the curvature to fit the best power law distribution. The left truncation should match with the minimum resolution of 3-D seismic data. The right truncation, on the other hand, is difficult to determine since it is related to the length of faults being beyond the target area. In this study, it is set to the point where the curvature deviates from the central straight line (Fig. 6c and d). According to the established fault length cumulative frequency distribution model and the relationship between fault length and maximum throw, we extrapolated the number of sub-seismic faults, and the length and throw of each sub-seismic fault (Table 1).

The rock mechanical parameters are obtained from triaxial experiments conducted on six core plug samples from B1 well (Table 2). The interpreted seismic faults and strata data were input into the Trap Tester software for the 3-D geo-mechanical simulation. There are two sets of fault systems in the study area. We simulated the two stages of the disturbed stress field when they formed. Since all the faults in the study area are normal faults, according to Anderson's model, we assumed that the direction of the minimum principal stress was

perpendicular to the fault strikes (that is 145.5° and 182.2° respectively). The magnitude of the applied strain was determined according to the extension amount of each period being 0.021 and 0.014 respectively. The preferred failure orientations and the maximum Coulomb shear stresses were then calculated with Equation (3) and Equation (4) (Fig. 7).

Finally, the distribution of sub-seismic faults is quantitatively predicted using the marked-point process stochastic technique (Fig. 8). The locations of the sub-seismic faults were constrained based on the distribution of the maximum Coulomb shear stress (Fig. 7). The larger the MCSS value of a grid point is, the greater probability of sub-seismic fault located there. The strikes of the sub-seismic fault were determined by the preferred failure orientation of the point which the center of the sub-seismic fault located. The length of each predicted sub-seismic fault was estimated according to the inverse function of the fault length cumulative frequency relationship (Equations (6) and (8)). The maximum throw of sub-seismic fault was obtained according to the relationship model between the maximum fault throw and the fault length (Equations (5) and (7)).

5. Discussion

5.1. Impact of the size of sub-seismic faults on waterflooding response time

The existence of sub-seismic faults and fractures significantly further complicates the reservoir heterogeneous (Rotevatn and Fossen, 2011; Gao et al., 2015). We use the response time to evaluate the effect of sub-seismic faults on the water flooding development. Response time refers to the time from the beginning of water injection to the time at which the production well has an obvious increase in output, which can be construed from the dynamic production curves. The throws of sub-seismic faults are calculated from Equations (5) and (7). To eliminate the effect of well spacing on the response time of different production wells, we also calculated the response time per unit distance (1000 m). According to the statistical relationship between sub-seismic fault

Table 2
Results of rock compression tests.

Sample No.	Diameter (mm)	Height (mm)	Failure load (kN)	Confining pressure (MPa)	Axial stress (MPa)	Young' modulus (GPa)	Poisson' ratio	Shear parameters
B1-1	25.38	53.18	42.06	0	73.41	34.52	0.244	Cohesion
B1-2	25.48	50.09	47.52	0	82.3	45.04	0.209	C = 18.89 MPa
B1-3	25.44	53.37	121.3	5	215.72	35.27	0.106	Internal friction angle
B1-4	25.46	56.18	145.35	10	262.09	41.8	0.132	$\varphi = 55.21^\circ$
B1-5	25.48	50.09	125.15	15	232.4	41.93	0.131	
B1-6	25.46	54.56	175.4	20	324.21	52.11	0.222	

throw and the response time, it is observed that the larger the sub-seismic fault is, the greater the response time and the ratio between response time and well spacing are (Fig. 9). This phenomenon is more distinct when the sub-seismic fault throw is larger than 6.5 m, where a significant positive correlation between response time and fault throw can be observed. The larger the sub-seismic fault throw, the more likely it will create a network of sealing sub-seismic faults. Thus, they can become effective barriers to waterflood front and causing longer flood response times. Even though the sub-seismic fault did not completely break the single sand body, affected by the cataclasis, clay smearing and late cementation, the permeability in the direction normal to the fault strike drops sharply, which also prolongs the response time.

5.2. Influence of sub-seismic faults on waterflood flow path

The existence of the sub-seismic faults also leads to a more tortuous flow of the injected water, which complicates the distribution of residual oil (Fig. 10). For instance, from the analysis of dynamic injection/production relationships, the water injection in well P3 is supposed to work on the production of well B4. Well B6 was completed recently and not yet to be deployed for production. Because the well B6 is not at the injection/production line of well P3 and well B4, if the reservoir between well P3 and well B4 is homogeneous and isotropic, the well B6 should be saturated with oil. However, the well B6 shows serious water flood even ahead of its production. This can be explained by the influence of sub-seismic faults. According to the prediction of sub-seismic faults (Fig. 8), there develops one sub-seismic fault between well P3 and well B4. This sub-seismic fault acts as a seepage barrier, which deviates the direction of injected water and accelerate the water breakthrough time at well B6.

5.3. Impact of sub-seismic faults on waterflood front advancement and remaining oil saturation

The influence of sub-seismic faults on water flooding development and remaining oil distribution depends on the relationship between the strikes of sub-seismic faults and the directions of injection/production

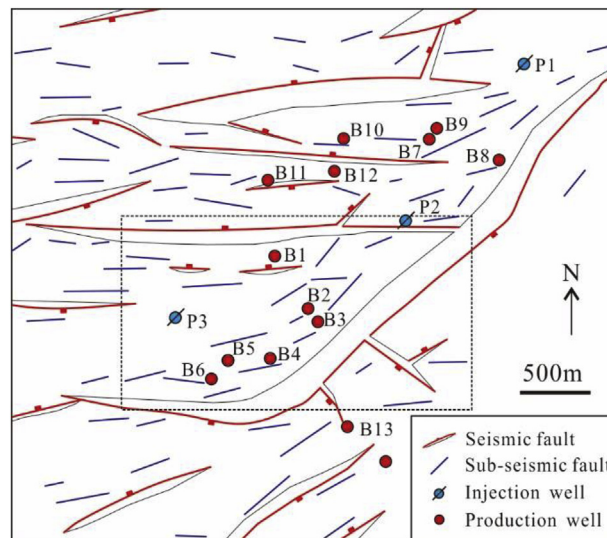


Fig. 8. Distribution of predicted sub-seismic fault of the second Member of Shahejie Formation (Es₂) of Bozhong 34–2 oilfield.

lines. According to the numerical simulation (Fig. 11), when the sub-seismic fault is normal to or intersected with the direction of injection/production lines at a high angle, there is a clear pressure gradient difference between the two sides of the faults: the pressure gradient drops sharply from the side of injection well to the side of production well. While the pressure gradient drops gradually when there is no sub-seismic fault or the sub-seismic faults are parallel to the injection/production lines.

When the sub-seismic faults are parallel to the directions of injection/production lines, the injected water flow quickly along the damage zones, shortening the response time. For instance, the existence of several sub-seismic faults parallel to the injection/production line of well P1 and well B9 makes the injected water from well P1 detectable in well B9 only in two months. However, the relatively low permeability

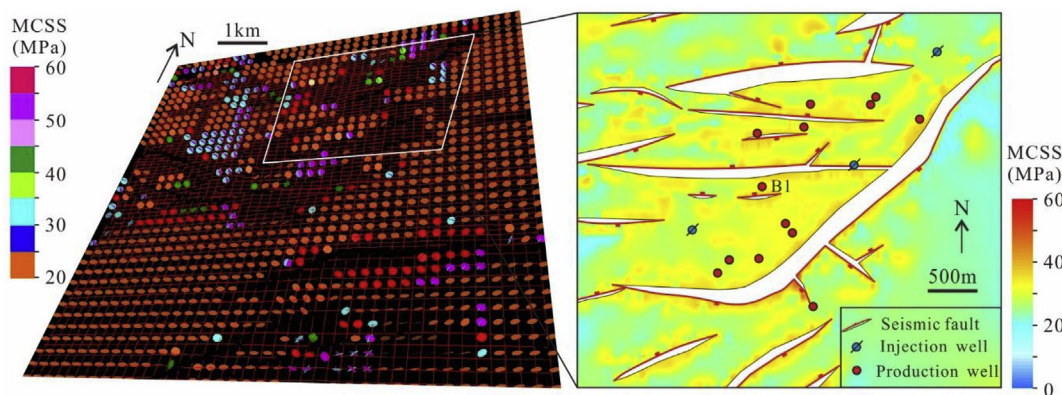


Fig. 7. Failure orientations and distribution of MCSS of the second Member of Shahejie Formation (Es₂) when the nearly E-W trending faults formed in Bozhong 34–2 oilfield. MCSS = Maximum Coulomb Shear Stress.

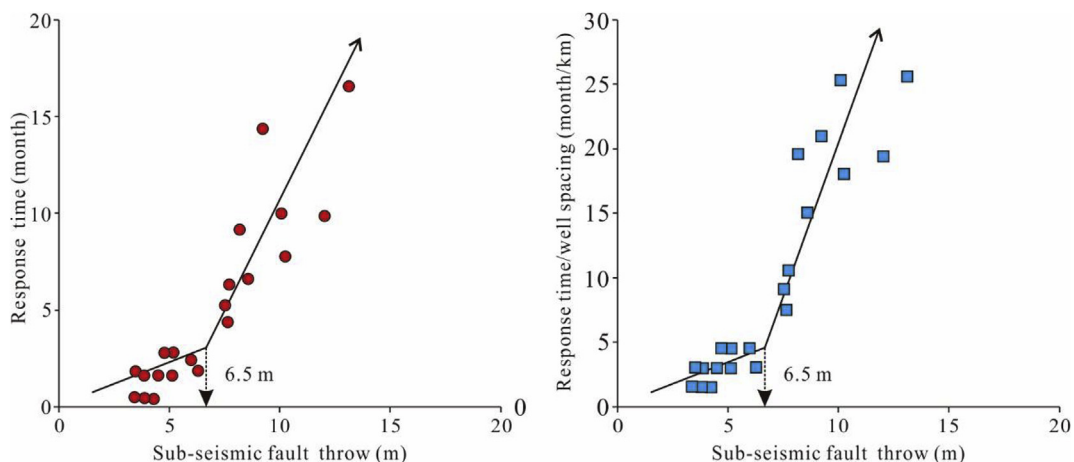


Fig. 9. (a) Relationship between the sub-seismic fault throw and the response time. (b) Relationship between the sub-seismic fault throw and the response time per km.

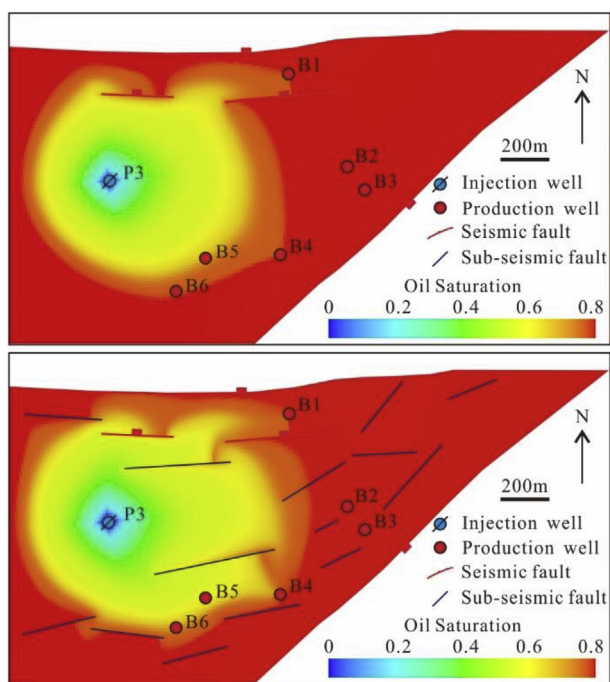


Fig. 10. Sweep efficiency maps showing the effects of sub-seismic faults on distribution of remaining oil. Well P3 is the injection well, Well B1 and B4 are the production wells. Other wells are completed recently and not yet to be deployed for production. See Fig. 8 for location of numeral simulation scope.

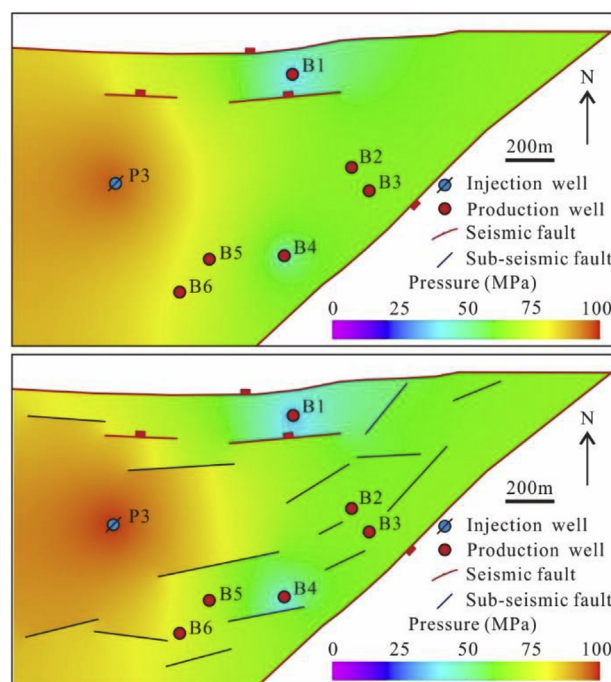


Fig. 11. Distributions of simulated reservoir pressure without sub-seismic faults (A) and with sub-seismic faults (B). Well P3 is the injection well, Well B1 and B4 are the production wells. Other wells are completed recently and not yet to be deployed for production. See Fig. 8 for location of numeral simulation scope.

areas of both sides of the sub-seismic faults tend to form remaining oil distribution. Therefore, when the sub-seismic faults are normal to the injection/production line, the remaining oil of the production well side is relatively rich. When the sub-seismic fault is parallel to the direction of injection/production line, both sides of the sub-seismic fault are rich in remaining oil. Combined with the sub-seismic fault simulation, we predicted the flooded areas in the second Member of Shahejie Formation (Fig. 12). In sum, three flooded areas are identified, i.e. P1, B10–P2 and P3–B4 flooded areas, which are consistent with the results from drilling reports.

6. Conclusion

Sub-seismic faults control the reservoir quality, hydrocarbon accumulation and water injection development. A quantitative prediction method was developed to predict the number, size, occurrence and

location of these sub-seismic faults based on the analysis of fault fractal growth patterns and 3-D geo-mechanical simulation. The number, length and throw of the sub-seismic faults were predicted by extrapolating the power law distribution of seismic fault parameters explained from 3-D seismic data. The occurrence and location of the sub-seismic faults was constrained based on a stochastic model deduced from the disturbed stress field near the seismic fault zone during faulting. This work shows that the distribution of sub-seismic faults can be effectively predicted by the combination of fractal theory and 3-D geo-mechanical simulation.

Sub-seismic faults play an important role in the reservoir connectivity, water injection development, and thus the distribution of remaining oil. The influence of the sub-seismic faults depends on the size of these faults and the relationships between their strikes and the directions of the injection/production lines. The large sub-seismic faults will tend to break the single sand body and worsen the lateral

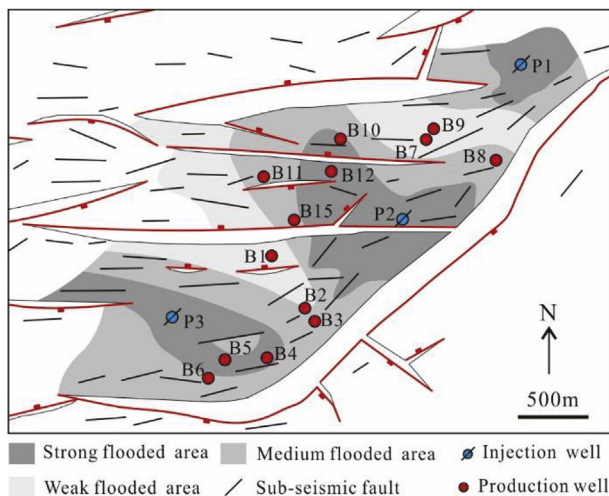


Fig. 12. Prediction of water flooding scenarios in the second Member of Shahejie Formation (E_{s2}) in Bozhong 34-2 oil field.

connectivity of the reservoir. When the sub-seismic faults are perpendicular to or intersected at a high angle with the direction of injection/production line, the injected water will change direction and flow along the sub-seismic faults due to the seepage barrier function of sub-seismic faults, which complicates the distribution of residual oil. When the sub-seismic faults are parallel to the directions of injection/production lines, the injected water flows quickly along the strikes of sub-seismic faults, shortens the effective time which leads to more remaining oil.

Acknowledgement

The authors would like to acknowledge the Research Institute of Petroleum Exploration and Development of PetroChina for providing Trap Tester software. This work is financially supported by the National Natural Science Foundation of China (grant nos. 41502124, U1562214 and 41572126), the Young Innovative Talents Training Program for Universities in Heilongjiang Province (grant no. UNPYSCT-2018043), the Natural Science Foundation of Heilongjiang Province (grant nos. QC2018043 and 41417837-8-13145), the China Postdoctoral Science Foundation (grant nos. 2018M631908 and 2015M581424) and Cultivating Fund of Northeast Petroleum University (grant nos. SCXHB201705 and 2017PYQZL-14).

References

Ackermann, R.V., Schlichte, R.W., 1997. Anticustering of small normal faults around larger faults. *Geology* 25 (12), 1127–1130.

Barnett, J.A.M., Mortimer, J., Rippon, J.H., Walsh, J.J., Watterson, J., 1987. Displacement geometry in the volume containing a single normal fault. *AAPG Bull.* 8 (71), 925–937.

Casini, G., Gillespie, P.A., Verges, J., Romaire, I., Fernandez, N., Casciello, E., Saura, E., Mehl, C., Homke, S., Embry, J.C., Aghajari, L., Hunt, D.W., 2011. Sub-seismic fractures in foreland fold and thrust belts: insight from the Lurestan Province, Zagros Mountains, Iran. *Petrol. Geosci.* 17 (3), 263–282.

Cosgrove, J.W., 2001. Hydraulic fracturing during the formation and deformation of a basin: a factor in the dewatering of low-permeability sediments. *AAPG Bull.* 85 (4), 737–748.

Damsleth, E., Sangoi, V., Aamodt, G., 1998. Sub-seismic faults can seriously affect fluid flow in the njord field off western Norway - a stochastic fault modeling case study. In: *SPE Annual Technical Conference and Exhibition*, New Orleans, Louisiana.

Ferrill, D.A., McGinnis, R.N., Morris, A.P., Smart, K.J., Sickman, Z.T., Bentz, M., Lehmann, D., Evans, M.A., 2014. Control of mechanical stratigraphy on bed-restricted jointing and normal faulting: eagle Ford Formation, south-central Texas. *AAPG Bull.* 98 (11), 2477–2506.

Fossen, H., 2010. Deformation bands formed during soft-sediment deformation: observations from SE Utah. *Mar. Petrol. Geol.* 27 (1), 215–222.

Fossen, H., Bale, A., 2007. Deformation bands and their influence on fluid flow. *AAPG Bull.* 91 (12), 1685–1700.

Fossen, H., Jonny, H., 2000. Possible absence of small faults in the Gullfaks Field, northern North Sea: implications for downscaling of faults in some porous

sandstones. *J. Struct. Geol.* 22 (7), 851–863.

Fu, X.F., Su, Y.P., Lyu, Y.F., Zhang, Y.F., Fu, G., 2007. Fractal characteristic and geological meaning of fault and fracture. *Earth Sci. (J. China Univ. Geosci.)* 32 (2), 227–234 (in Chinese with English abstract).

Fu, X.F., Sun, B., Wang, H.X., Meng, L.D., 2015. Fault segmentation growth quantitative discrimination and its application on hydrocarbon accumulation research. *J. China Inst. Min. Technol.* 44 (02), 258–268 (in Chinese with English abstract).

Fu, X.F., Xu, P., Wei, C.Z., Lyu, Y.F., 2012. Internal structure of normal fault zone and hydrocarbon migration and conservation. *Earth Sci. Front.* 19 (6), 200–212 (in Chinese with English abstract).

Gao, S., Zeng, L.B., Ma, S.Z., He, Y.H., Gong, L., Zhao, X.Y., Xu, W.G., Tang, X.M., 2015. Quantitative prediction of fractures with different directions in tight sandstone reservoirs. *Nat. Gas Geosci.* 26 (03), 427–434 (in Chinese with English abstract).

Gauthier, B.D.M., Lake, S.D., 1993. Probabilistic modeling of faults below the limit of seismic resolution in Pelican Field, North sea, offshore United Kingdom. *AAPG Bull.* 77 (5), 761–777.

Gong, L., Zeng, L.B., Miao, F.B., Wang, Z.S., Wei, Y., Li, J., Zu, K.W., 2012. Application of fractal geometry on the description of complex fracture systems. *J. Hunan Univ. Sci. Technol. (Nat. Sci. Ed.)* 27 (4), 6–10 (in Chinese with English abstract).

Gong, L., Gao, S., Fu, X.F., Chen, S.M., Lyu, B.Y., Yao, J.Q., 2017. Fracture characteristics and their effects on hydrocarbon migration and accumulation in tight volcanic reservoirs: a case study of the Xujiaweizi fault depression, Songliao Basin, China. *Interpretation* 5 (4), 57–70.

Gudmundsson, A., Simmenes, T.H., Larsen, B., Philipp, S.L., 2010. Effects of internal structure and local stresses on fracture propagation, deflection, and arrest in fault zones. *J. Struct. Geol.* 32 (11), 1643–1655.

Hooker, J.N., Laubach, S.E., Marrett, R., 2013. Fracture-aperture size-frequency, spatial distribution, and growth processes in strata-bounded and non-strata-bounded fractures, Cambrian Mesón Group, NW Argentina. *J. Struct. Geol.* 54, 54–71.

Hooker, J.N., Laubach, S.E., Marrett, R., 2014. A universal power-law scaling exponent for fracture apertures in sandstones. *Geol. Soc. Am. Bull.* 126 (9–10), 1340–1362.

Jiang, F.J., Pang, X.Q., 2011. Quantitative evaluation of hydrocarbon resource potential and its distribution in the Bozhong Sag and surrounding areas, Bohai Bay Basin. *Petrol. Explor. Dev.* 38 (1), 23–29.

Kim, Y., Peacock, D.C.P., Sanderson, D.J., 2004. Fault damage zones. *J. Struct. Geol.* 26 (3), 503–517.

King, G., 1983. The accommodation of large strains in the upper lithosphere of the earth and other solids by self-similar fault systems: the geometrical origin of b-value. *Pure Appl. Geophys.* 121 (5), 761–815.

Laubach, S.E., Eichhubl, P., Hargrove, P., Ellis, M.A., Hooker, J.N., 2014. Fault core and damage zone fracture attributes vary along strike owing to interaction of fracture growth, quartz accumulation, and differing sandstone composition. *J. Struct. Geol.* 68, 207–226.

Lohr, T., Krawczyk, C.M., Tanner, D.C., Samiee, R., Endres, H., Thierer, P.O., Oncken, O., Trappe, H., Bachmann, R., Kukla, P.A., 2008. Prediction of subseismic faults and fractures: integration of three-dimensional seismic data, three-dimensional retro-deformation, and well data on an example of deformation around an inverted fault. *AAPG Bull.* 92 (4), 473–485.

Luo, Q.Y., Gong, L., Qu, Y.S., Zhang, K.H., Zhang, G.L., Wang, S.Z., 2018. The tight oil potential of the Lucaogou Formation from the southern Junggar Basin, China. *Fuel* 234, 858–871.

Maerten, L., Gillespie, P., Daniel, J., 2006. Three-dimensional geomechanical modeling for constraint of subseismic fault simulation. *AAPG Bull.* 90 (9), 1337–1358.

Marrett, R., Ortega, O.J., Kelsey, C.M., 1999. Extent of power-law scaling for natural fractures in rock. *Geology* 27 (9), 799–802.

Meng, L.D., Fu, X.F., Wang, Y.C., Zhang, X.L., Lyu, Y.F., Jiang, Y.B., Yang, H.S., 2014. Internal structure and sealing properties of the volcanic fault zones in Xujiaweizi Fault Depression, Songliao Basin, China. *Petrol. Explor. Dev.* 41 (2), 165–174.

Odling, N.E., 1997. Scaling and connectivity of joint systems in sandstones from western Norway. *J. Struct. Geol.* 19 (10), 1257–1271.

Ortega, O., Marrett, R., 2000. Prediction of macrofracture properties using microfracture information, Mesaverde Group sandstones, San Juan basin, New Mexico. *J. Struct. Geol.* 22 (5), 571–588.

Packard, J.J., Al-Aasm, I., Samson, I., Berger, Z., Davies, J., 2001. A Devonian hydrothermal chert reservoir: the 225 bcf Parkland field, British Columbia, Canada. *AAPG Bull.* 85 (1), 51–84.

Peacock, D.C.P., Nixon, C.W., Rotevatn, A., Sanderson, D.J., Zuluaga, L.F., 2017. Interacting faults. *J. Struct. Geol.* 97, 1–22.

Rotevatn, A., Fossen, H., 2011. Simulating the effect of subseismic fault tails and process zones in a siliciclastic reservoir analogue: implications for aquifer support and trap definition. *Mar. Petrol. Geol.* 28 (9), 1648–1662.

Sanderson, D.J., Nixon, C.W., 2015. The use of topology in fracture network characterization. *J. Struct. Geol.* 72, 55–66.

Schueller, S., Braathen, A., Fossen, H., Tveranger, J., 2013. Spatial distribution of deformation bands in damage zones of extensional faults in porous sandstones: statistical analysis of field data. *J. Struct. Geol.* 52, 148–162.

Steen, Y., Arild, A., 1999. Effects of lithology on geometry and scaling of small faults in Triassic sandstones, East Greenland. *J. Struct. Geol.* 21 (10), 1351–1368.

Strijker, G., Bertotti, G., Luthi, S.M., 2012. Multi-scale fracture network analysis from an outcrop analogue: a case study from the Cambro-Ordovician clastic succession in Petra, Jordan. *Mar. Petrol. Geol.* 38 (1), 104–116.

Walsh, J.J., Watterson, J., Heath, A., Gillespie, P.A., Childs, C., 1998. Assessment of the effects of sub-seismic faults on bulk permeabilities of reservoir sequences. *Geol. Soc., London, Special Publications* 127, 99–114.

Wang, X.X., Hou, J.G., Song, S.H., Wang, D.M., Gong, L., Ma, K., Liu, Y.M., Li, Y.Q., Yan, L., 2018. Combining pressure-controlled porosimetry and rate-controlled porosimetry

- to investigate the fractal characteristics of full-range pores in tight oil reservoirs. *J. Petrol. Sci. Eng.* 171, 353–361.
- Xu, S., Hao, F., Xu, C.G., Wang, Y.B., Zou, H.Y., Gong, C.L., 2015. Differential compaction faults and their implications for fluid expulsion in the northern Bozhong Subbasin, Bohai Bay Basin, China. *Mar. Petrol. Geol.* 63, 1–16.
- Zhao, L., Li, L., 2016. The extensional pattern and dynamics of Bohai Bay basin in Late Mesozoic-Cenozoic. *Chin. Geol.* 43 (2), 470–485 (in Chinese with English abstract).
- Zeng, L.B., Liu, H.T., 2010. Influence of fractures on the development of low-permeability sandstone reservoirs: a case study from the Taizhao district, Daqing Oilfield, China. *J. Petrol. Sci. Eng.* 72 (1–2), 120–127.
- Zeng, L.B., Su, H., Tang, X.M., Peng, Y.M., Gong, L., 2013. Fractured tight sandstone oil and gas reservoirs: a new play type in the Dongpu depression, Bohai Bay Basin, China. *AAPG Bull.* 97 (3), 363–377.